Gravity Wave Morphology During the 2018 Sudden Stratospheric Warming Simulated by a Whole Neutral Atmosphere General Circulation Model

S. Watanabe[1], D. Koshin[1,2], S. Noguchi[1] and K. Sato[2]

[1] Japan Agency for Marine-Earth Science and Technology (JAMSTEC), Yokohama, Japan.

[2] Department of Earth and Planetary Science, Graduate School of Science, The University of Tokyo, Tokyo, Japan.

Corresponding author: Shingo Watanabe (wnabe@jamstec.go.jp)

Key Points:

- Gravity waves during the 2018 sudden stratospheric warming were simulated using a whole neutral atmosphere general circulation model.
- Three-dimensional visualization analyses revealed their characteristic morphology around the dramatically evolving polar vortex.
- Paths of gravity waves near the Canadian sub-vortex were estimated by ray-tracing, highlighting long-distance gravity wave propagation.

Abstract

Atmospheric gravity waves (GWs) during the February 2018 sudden stratospheric warming (SSW) were simulated using the T639L340 whole neutral atmosphere general circulation model. Their characteristic morphology around the drastically evolving polar vortex was revealed by three-dimensional (3D) visualization and ray-tracing analyses. The 3D morphology of simulated GWs was described for the three key days that represent the pre-SSW, the mature stage for the vortex splitting, and the late SSW. The combination of strong winds along the polar vortex edge and underneath the tropospheric winds with similar wind directions consisted of the deep waveguide for the upward-propagating GWs, forming GW hot spots in the middle atmosphere. The GW hot spots associated with the development of the SSW were limited to North America and Greenland, and they included the typical upward-propagating orographic GWs with relatively long vertical wavelengths. Different types of characteristic GW signatures were also recognized around the Canadian sub-vortex (CV). The GWs having short vertical wavelengths formed near the surface and obliquely propagated over long distances along the CV winds. The non-orographic GWs with short vertical wavelengths formed in the middle stratosphere through the spontaneous adjustment of flow imbalance around the CV. Those GWs cyclonically ascended into the mesosphere along CV winds.

Plain Language Summary

Atmospheric gravity waves (GWs) have three-dimensional phase structures and propagate three-dimensionally from their sources. Examples include flow over mountains, convection, fronts, and dynamically imbalanced flow systems. For the first time, we simulated and visualized their global morphology from the surface to an altitude of ~100 km by focusing on the February 2018 sudden stratospheric warming event, when the stratospheric polar vortex split into two sub-vortices. The most interesting findings in the three-dimensional and ray-tracing analyses are the formation of narrow GW hotspots along the south to east rim of the Canadian sub-vortex (CV) and the cyclonical ascent of GW packets around the edge of the CV.

1. Introduction

Atmospheric gravity waves (GWs) are small-scale wave disturbances that propagate in a three-dimensional (3D) manner from their sources; examples include flow over mountains, convection, fronts, and dynamically imbalanced flow systems (Fritts & Alexander, 2003). In the troposphere, their horizontal propagation is often visualized as stripe clouds aligned perpendicular to flows blowing over mountains. Although this mode is invisible, they also propagate vertically and play crucial roles in the dynamics and energy budget of the Earth's stratosphere, mesosphere, and lower thermosphere. Their propagation is strongly influenced by the background environment, especially horizontal and vertical shears in winds and static stability, as described by the GW ray-tracing equation (e.g., Marks & Eckermann, 1995).

Changes in the stratospheric circulation associated with sudden stratospheric warming (SSW), such as deformation, displacement, breakup, and temporary disappearance of the stratospheric polar vortex, cause substantial changes in the propagation environment of GWs. Limpasuvan et al. (2011) performed mesoscale simulations of GWs during the 2008-2009 SSW and revealed a dominance of westward-propagating orographic GWs along the edge of the polar vortex prior to the SSW, which was greatly reduced after the occurrence of the SSW. During the SSW, they found westward- and eastward-propagating GWs in the polar region and attributed their possible generation mechanisms to a flow adjustment process in the stratosphere or secondary GW breaking. Their mesoscale model had a horizontal resolution of 10 km and a vertical resolution of 400 m. The simulation domain was the poleward side of 50°N and an altitude of 0-55 km. Their study inspired us to perform similar GW simulations during an SSW using a wider simulation domain of global and 0- to 150-km altitude, and to illustrate the characteristic morphology of GWs by using 3D visualization and ray-tracing analyses. This was made possible by advances in the computing environment and the development of our own data assimilation system for the whole neutral atmosphere (Koshin et al., 2020, 2021), which can be used to constrain large-scale meteorological fields of a higher-resolution GW-permitting general circulation model (GCM).

Recently, the importance of 3D propagation of GWs has been revealed by high-resolution modeling studies (e.g., Sato et al., 2012; Shibuya et al., 2017) and observational studies (e.g., Wright et al., 2017; Perrett et al., 2021). The GW parameterization used in general climate

models, which cannot resolve GWs, conventionally assumes propagation in a vertical one-dimensional column, but another type of scheme that considers 3D propagation has been proposed (Song & Chun, 2008; Amemiya & Sato, 2016). However, most recent studies have focused on the mid latitudes of the southern hemisphere, and there are few studies on the 3D propagation of GWs in the Northern Hemisphere (NH), which has more complex topography and flow fields. In this context, the 3D propagation of GWs during an SSW event, which this case study demonstrates, is expected to be a good reference example for further development of GW parameterizations.

We performed GW simulations using a whole neutral atmosphere GCM having a 20-km horizontal resolution and a 300-m vertical resolution that extends from the surface to an altitude of 150 km. Okui et al. (2021) discussed the ability of the model to simulate dominant GWs that have been observed in the middle atmosphere by atmospheric radars and meteor radars. Overall, the model can reproduce a realistic amplitude and phase structure of GWs, as well as their effects on the large-scale flows and thermal structures under the limitation of horizontal and vertical resolutions. The dependency of GW morphology on the model's horizontal resolution will be briefly discussed in this study.

In this paper, we focus on an SSW that occurred in February 2018. This SSW is classified in the same broad category as the 2008-2009 SSW as a polar vortex splitting type (e.g., Charlton & Polvani, 2007), but it is unique in that 1) the Canadian sub-vortex (CV) was larger and more stable than the Eurasian sub-vortex and 2) the latter SSW was characterized by the Arctic region being covered by deep easterly winds from the troposphere to the mesosphere (Harada et al., 2019). One of the reasons for choosing this SSW event is that it is the target of an intensive observational campaign in the Interhemispheric Coupling Study by Observations and Modeling (ICSOM), and the results of this simulation are expected to lead to the development of various scientific perspectives in future studies (https://pansy.eps.s.u-tokyo.ac.jp/en/projects/icsom/index.html).

This paper is structured as follows. The model and experimental design and the 3D visualization and ray-tracing analysis methods are described in Section 2. In Section 3, the 3D morphology of simulated GWs is illustrated during three key days, which represent the pre-SSW, the mature stage for the vortex splitting, and the late SSW. Section 4 focuses on the origin and

3D propagation pathways of GWs based on the ray-tracing analyses. Discussion and a summary are given in Section 5.

2. Methods

2.1 Model and Experimental Design

Gravity wave simulations were performed using the Japanese Atmospheric GCM for Upper Atmosphere Research (Watanabe & Miyahara, 2009). The model extends from the surface to the lower thermosphere (≈150 km) and contains 340 vertical layers with a constant log-pressure height interval of 300 m throughout the middle atmosphere (Watanabe et al., 2015). It is a global spectral model, and a T639 triangle truncation was used in this study, which corresponds to a minimum resolvable horizontal wavelength of ~60 km (a latitude interval of 0.1875°). No parameterization for sub-grid-scale GWs was used in this study.

The model is initialized using a data assimilation data set for the whole neutral atmosphere created by the Japanese Atmospheric GCM for Upper Atmosphere Research-Data Assimilation System (JAGUAR-DAS; Koshin et al., 2020, 2021). A 3-day spectral nudging was performed in the initialization in which the low total horizontal wavenumber components (n = 0-40) are relaxed to the assimilation data, while higher horizontal wavenumber components (n = 41-639), including GWs, freely evolve. The ERA5 re-analysis data set (Hersbach et al., 2020) with a 0.25° horizontal resolution was used to constrain n = 0-40 components in the troposphere, where JAGUAR-DAS with T42 (2.8125°) horizontal resolution is less reliable. Afterwards, 4-day free-running simulations were performed to include three key days, that is, 1) 4 February 2018, representing pre-SSW conditions; 2) 11 February 2018, just after the vortex splitting; and 3) 15 February 2018, representing late SSW conditions. The model can successfully hindcast the temporal evolution of large-scale dynamics of the SSW during the independent 4-day periods. Note that individual GWs are neither initialized nor hindcasted but are spontaneously generated in the model in harmony with the hindcasted large-scale fields and model's boundary conditions, such as topography and sea surface temperatures.

2.2 3D Visualization of GWs

The 3D visualization analyses of GWs were performed using the Visualization and Analysis Platform for Ocean, Atmosphere, and Solar Researchers (VAPOR) software, version 2.6.0 (Li et al., 2019). The simulation outputs were saved in 1-hour intervals as 1-hour averages

and converted into the VDF (VAPOR data format for version 2) format. Table 1 summarizes the output and diagnostic variables visualized with VAPOR in this study. The 3D distribution and phase structures of GWs are identified by isosurface visualizations with a specific magnitude of DIV $\equiv \exp(-z/4H) \times \nabla \cdot \boldsymbol{v}_{\mathrm{h}}$, where H denotes the scale height and $\boldsymbol{v}_{\mathrm{h}}$ represents unfiltered horizontal winds.

Table 1. Output and diagnostic variables used in this study. ND denotes non-dimensional variable.

Variable name	Description	Unit
DIV	Unfiltered horizontal wind divergence scaled by log-pressure height	s^{-1}
DTCND	Diabatic heating rate from sub-grid scale parameterizations for cumulus and large-scale condensation	$K\ s^{-1}$
MPV	Modified potential vorticity computed with the large-scale (n = 0-20) horizontal winds and potential temperature (Matthewman et al., 2009)	$10^{-6}\ K\ m^2\ s^{-1}\ kg^{-1}$
RoL	Local Rossby number computed with the large-scale horizontal winds (Sato & Yoshiki, 2008)	ND
U	Large-scale (n = 0-20) eastward winds	$m\ s^{-1}$
V	Large-scale (n = 0-20) northward winds	$m\ s^{-1}$
ZLEV	Log-pressure height computed with the model's vertical coordinate system and the standard surface pressure	m

Due to the limitation of the software, the model's native grid points (x:1,920, y:960, and z:340) were down-sampled to (x:1,920, y:480, and z:170), where the latitudinal domain is limited to the NH and the number of vertical layers is halved. The vertical down-sampling might be a cause of noisy structures in the 3D visualization of GWs, although it does not affect the conclusions in this study.

2.3 Ray-tracing Analysis

To estimate the origins and destinations of GWs identified in the 3D analysis, backward and forward ray-tracing calculations were performed. A couple of modifications were applied to

the 3D nonhydrostatic ray-tracing equations defined by Marks and Eckermann (1995) to examine the 3D propagation of GWs in the hydrostatic GCM with a finite vertical resolution. The hydrostatic approximation was applied, and ray tracing was terminated when the vertical wavelength became shorter than a cut-off of 2 km, considering the model's effective vertical resolution. The latter condition is important to avoid unrealistic backward ray tracing, namely over propagation, of GWs generated from in-situ dynamics, such as GWs emitted from deformed large-scale flows and secondary GWs emitted from the wave forcing associated with breaking orographic GWs. As for the bottom boundary condition, to avoid a spurious GW reflection at the surface, the ray tracing was terminated when the ray position descended below 2 km. The hourly average large-scale (n = 0-20) horizontal winds, density scale height, and Brunt–Väisälä frequency were used as the background conditions. A time step of 60 seconds was used for the ray-tracing time integration.

In this study, a handful of characteristic GWs were visually identified from a certain log-pressure height surface in the 3D analysis. The horizontal and vertical wavenumbers of the GWs were estimated by combining the latitude-height and longitude-height cross sections, which were then used to estimate a full set of initial conditions for the ray-tracing analysis. Indeed, many sources of uncertainty exist in the estimation of geometric wavenumbers, which leads to wrong estimations of GW rays compared with the actual four-dimensional behavior of simulated GW packets. The dispersion of GWs, overlap of multiple monochromatic GWs, horizontal and/or vertical shears in background horizontal winds, and spatial variations of the background static stability and density scale height make the estimation difficult. A trial-and-error approach with visual inspection was used to identify likely correct initial GW parameters from a few candidates according to the consistency between the estimated GW rays and the behavior of simulated GW signatures. The resultant backward and forward GW rays were saved as 3D scalar variables – GWbwd and GWfwd, respectively – and converted into the VDF format, which was then visualized with VAPOR along with the GW signatures (DIV).

3. Simulated GWs During Key Dates

3.1 Pre-SSW: 4 February 2018

Figure 1 shows the instantaneous 3D morphology of simulated GWs around the NH polar vortex at 00:00UT on 4 February 2018 during the pre-SSW period. The top, slanted, and side views from the south are displayed to provide the least 3D information of the GW phase structures. The body of the polar vortex at a height of 20-40 km is approximately illustrated as a white transparent isosurface of 30 PVU, whose center is displaced to Europe. Large-amplitude GWs are visualized with a DIV = -6×10^{-5} isosurface, which is colored with the local background U. Here, only negative DIV values are visualized because of the ease of estimating wavelengths and in seeing the background GW signatures behind the foreground. Apparently, the strong winds around the polar vortex provide a favorable environment for upward-propagating GWs.

In the region from the North Atlantic to western Eurasia, GWs having phase structures tilting westward with increasing altitude are dominant. These GWs are propagating upward and westward against the background eastward winds. They typically have horizontal wavelengths of 90-300 km and vertical wavelengths of 5-30 km. The vertical wavelengths increase with height due to a Doppler shift by increasing eastward winds. The GW signatures disappear at a height of 70-90 km due to discontinuous decrease of wave amplitudes associated with wave-breaking. Several sources of GWs are suggested in the troposphere, as indicated by the arrows. Figure 1b shows north-south-oriented, line-shaped moist diabatic heating over the central North Atlantic as indicated by the yellow isosurface, which seems to emit non-orographic GWs having phase lines parallel to the isosurface. The north-south-oriented, arc-shaped GW signature over west Ireland was probably emitted from the upper-level front near the tropopause through a spontaneous adjustment. Figure 1c shows the signatures of orographic GWs over northeastern Canada, the southern tip of Greenland, Iceland, Svalbard, and central Europe.

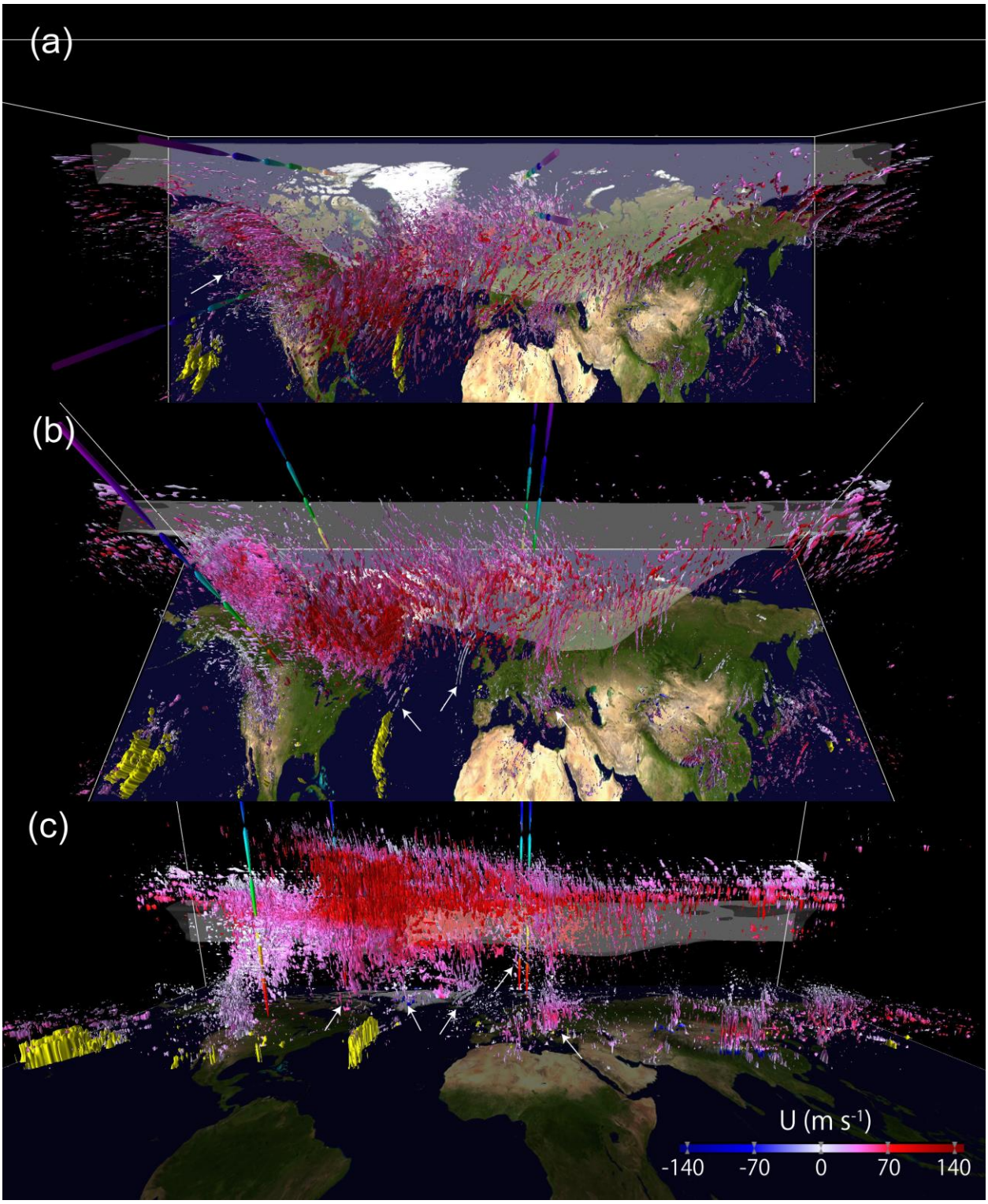

Figure 1. 3D view of GW signatures in the T639L340 GCM at 00:00UT on 4 February 2018. The isosurface of DIV = -6×10^{-5} is displayed, which is colored by the local background eastward winds (U). Also shown are the yellow isosurface of moist diabatic heating, DTCND = 1 K d^{-1};

212 the white transparent isosurface of the modified potential vorticity, MPV = 30 PVU between 20-
213 and 40-km; and vertical scales indicating 0-20 km (red), 20-40 km (yellow), 40-60 km (green),
214 60-80 km (light blue), 80-100 km (blue), and >100 km (purple). The location of the vertical scale
215 is arbitrary, and it is placed at a convenient and unobtrusive point for viewing GWs.

216

217 In the region from Alaska to northwestern Canada, GWs having an east-west phase
218 orientation are dominant (Figure 1a). Figure 2 shows a close-up view of this region from the
219 west. The GWs are orographic, have phase structures tilting northward with increasing altitude,
220 and propagate upward and northward against the background southeastward winds. They have
221 horizontal wavelengths of 150-200 km and vertical wavelengths of 10-20 km, dissipating at
222 about 60-65 km. Their horizontal wavelengths roughly correspond to the width of north-south
223 slope of the east-west-oriented mountains in this region. The vertical wavelength at 35 km
224 coincides with the theoretical prediction for non-rotational and hydrostatic GWs, namely
225 $\boldsymbol{\lambda_z = 2\pi|U|/N}$, where $\boldsymbol{|U|}$ and $\boldsymbol{N}$ denote the background wind speed parallel to the orientation
226 of topography and Brunt–Väisälä frequency, respectively. Here, $\boldsymbol{\lambda_z}$ = 11 km is obtained by
227 substituting $\boldsymbol{|U|}$ = 36.8 m s^{-1} and $\boldsymbol{N}$ = 2.10 × 10^{-2} s^{-1}.

228

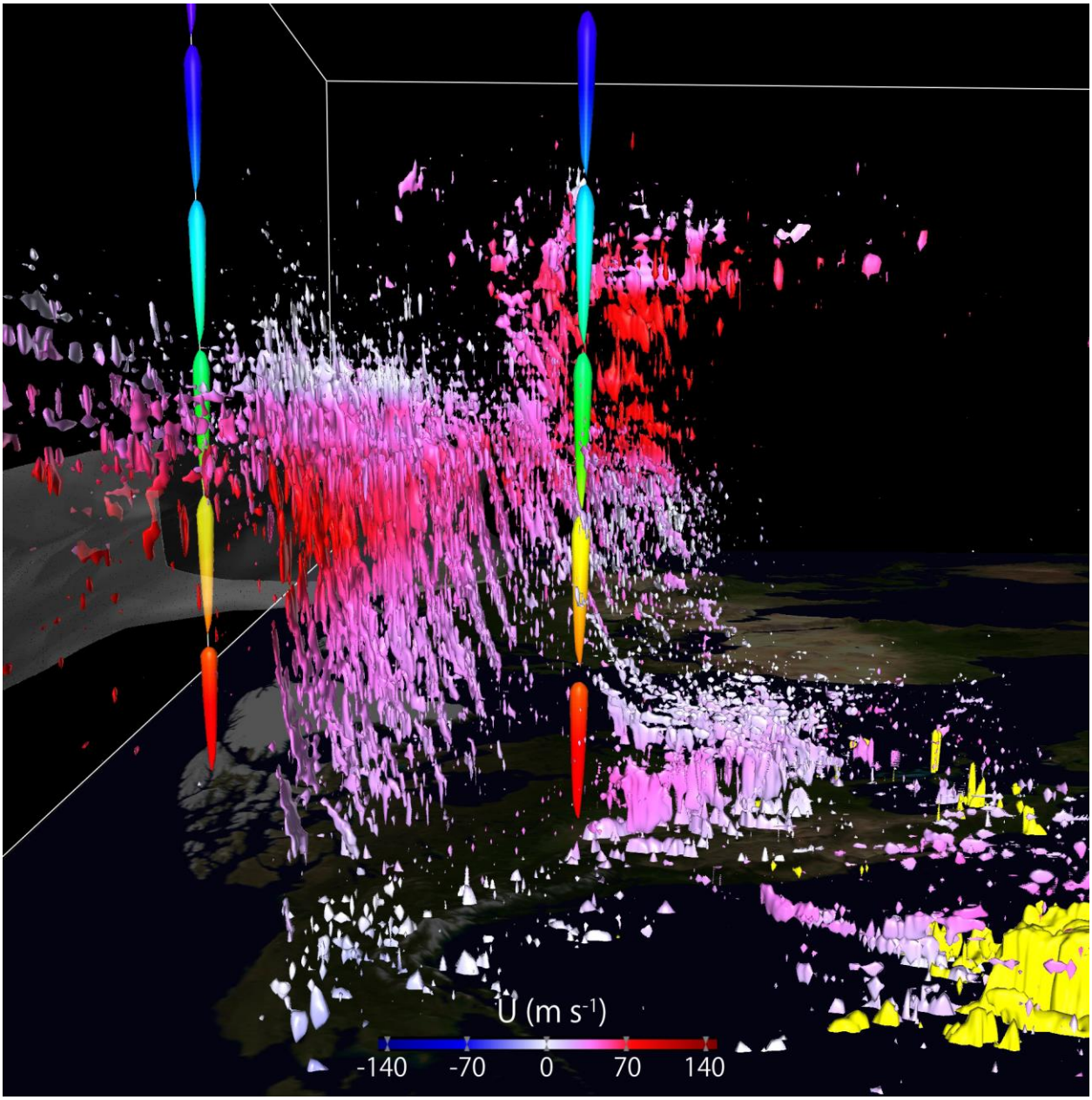

Figure 2. The same as Figure 1 but for GW signatures over Alaska as seen from the west.

GW signatures are less prominent in the region from central Eurasia to the Northwest Pacific. This is attributable to the difference in horizontal wind direction between the troposphere and stratosphere, which prohibits upward propagation of quasi-stationary GWs. Figure 3a demonstrates such an environment by comparing geopotential height contours at 5 km and 30 km.

In the mid-latitude region from East Asia to the central North Pacific, well-developed synoptic-scale disturbances at 5 km are covered by a weak wind region associated with the stratospheric Aleutian high at 30 km. This contrasts with the other regions described above. GW signatures seen above 20 km in this region are presumed to be generated in situ.

Figure 3b and 3c compares the geopotential height distributions at 30, 50, and 70 km, revealing that the center of the polar vortex rapidly inclines to the southwest between 50 and 70 km. Therefore, the orographic GWs in the Alaska to northwest Canada region seen in Figure 2 approach their critical levels near a height of 60-65 km. Meanwhile, the vertical shear of horizontal winds is relatively small in the North Atlantic to western Eurasia region, allowing GWs to propagate to 70 km and above.

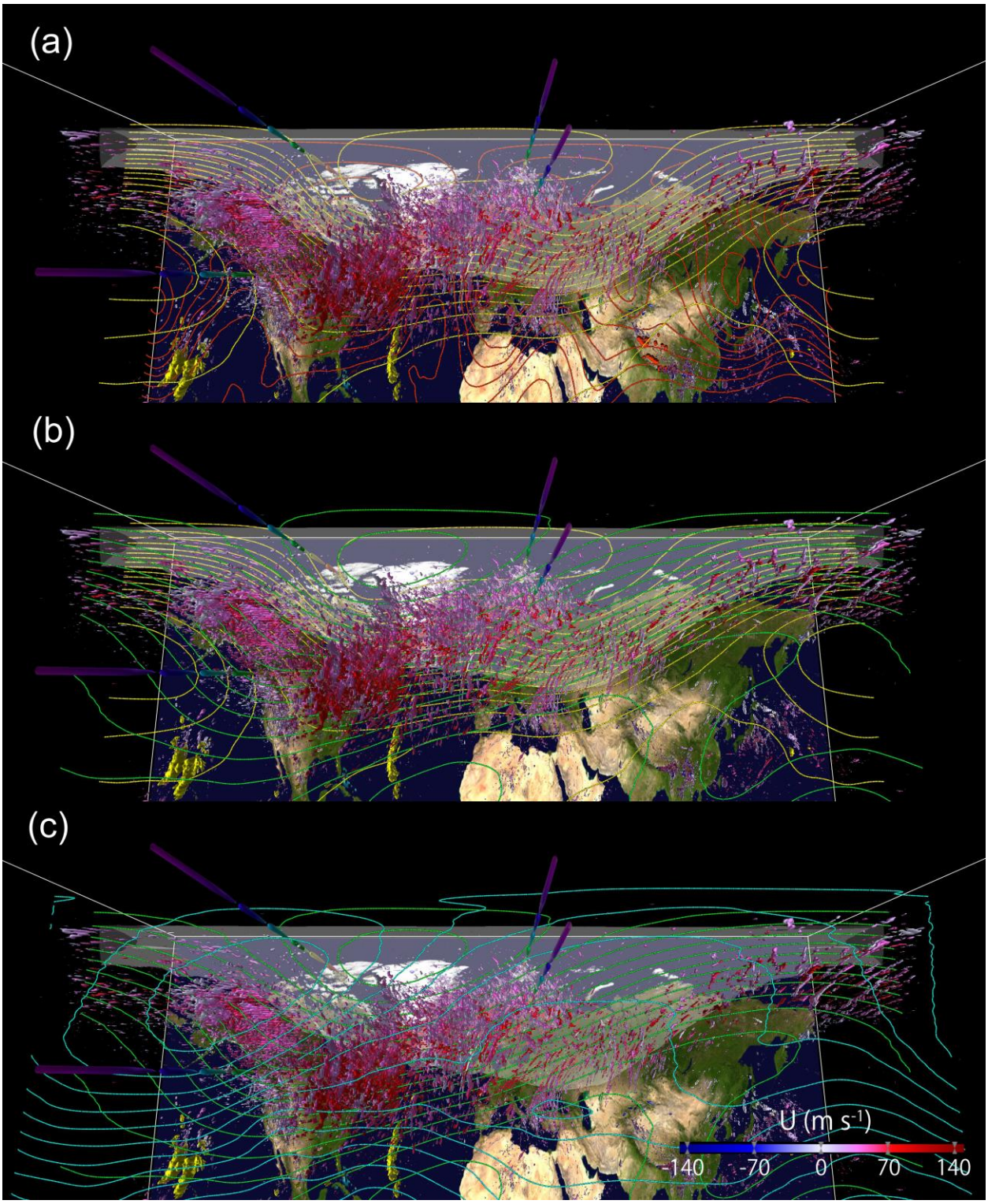

Figure 3. The same as Figure 1 but with contours of geopotential height. Geopotential height contours are compared at (a) 5 km (red) and 30 km (yellow), (b) 30 km (yellow) and 50 km (green), and (c) 50 km (green) and 70 km (light blue).

3.2 Vortex Splitting: 11 February 2018

Figures 4 and 5 are the same 3D views as Figures 1 and 3, respectively, but for 20:00UT on 11 February 2018, after the polar vortex split. The CV widely covers North America and western Greenland, and gradually tilts southwestward in the upper stratosphere and mesosphere. It contains many interesting GW signatures. The first thing that is noticeable is that the region where GWs propagate from the troposphere to the mesosphere is limited to areas around the CV, while in other regions, the GW signatures between the troposphere-lower stratosphere and the upper stratosphere-mesosphere are clearly separated. Figure 5 shows that the wind direction differs between the troposphere and stratosphere outside the CV area. Wide areas over Europe, northern Eurasia, and East Asia are covered by an anticyclone in the lower stratosphere that prevents upward propagation of quasi-stationary GWs generated in cyclonic flows in the troposphere.

A closer look at the CV area reveals that the tropospheric sub-tropical jet coincides with the south to east rim of the CV, and they consist of a deep cyclonic jet stream, which makes a favorable environment, a so-called wave guide, for upward-propagating GWs. There, orographic GWs having long vertical wavelengths and phase structures that tilt westward with increasing height can be identified near the Rocky Mountains, the northeast coast of the Labrador Peninsula, and the southern tip of Greenland, which propagate into the mesosphere. They typically have horizontal and vertical wavelengths of 90-180 km and 5-30 km, respectively. Interestingly, GWs having short vertical wavelengths of ~2-4 km are also found downstream of the Rocky Mountains, and their phase lines tilt northeastward with increasing height.

In the northern part of the CV, the prevailing eastward wind in the troposphere is covered by the westward wind in the stratosphere. Such a wind structure prevents the upward propagation of quasi-stationary GWs from the troposphere. Signatures of GWs that have short vertical wavelengths of 2-4 km are aligned parallel to the northeast to north rim of the CV in the upper stratosphere and lower mesosphere. They are probably generated by spontaneous adjustment due to flow imbalances at those altitudes. The wave parameters, origin, and propagation path of GWs

around the CV during this vortex splitting period are of central interest in this study and are discussed further in Section 4.

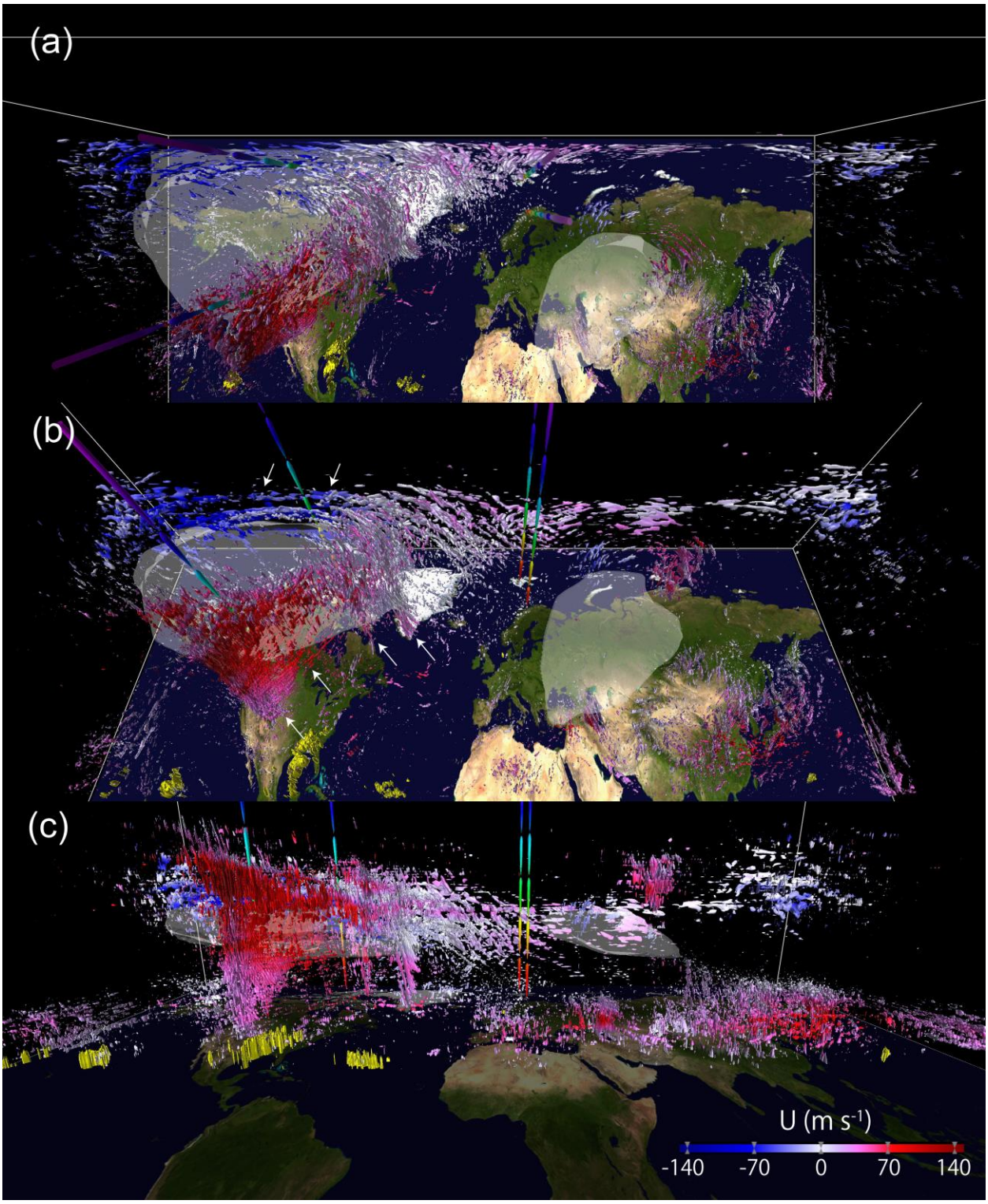

Figure 4. The same as Figure 1 but at 20:00UT on 11 February 2018.

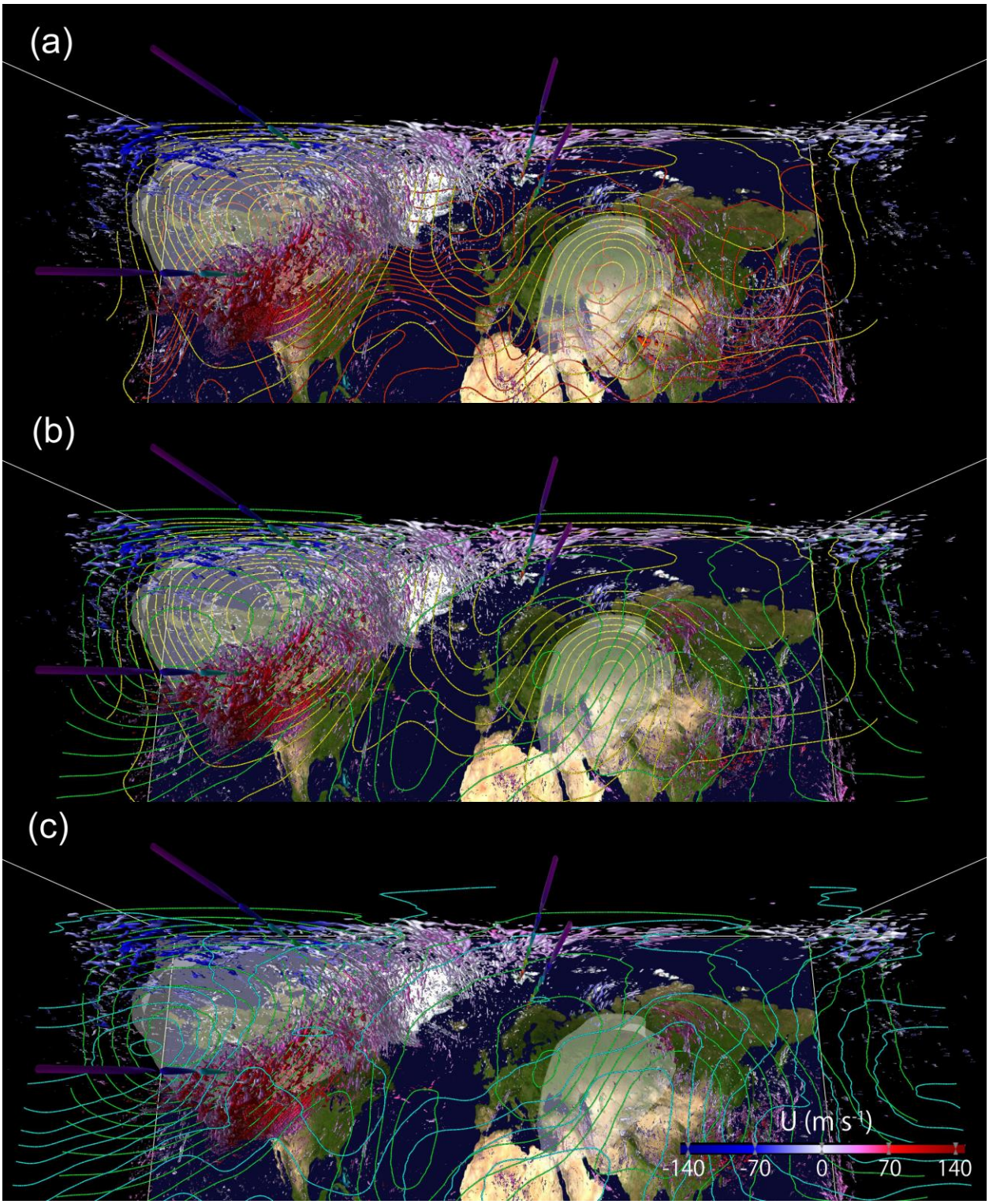

Figure 5. The same as Figure 3 but at 20:00UT on 11 February 2018.

3.3 Late SSW: 15 February 2018

Figures 6 and 7 are the same 3D views as Figures 1 and 3, respectively, but for 15:00UT on 15 February 2018, 5 days after the SSW occurred. Now, the CV strongly inclines to the southwest, and therefore the south to east rim of the CV no longer forms a deep waveguide for upward-propagating orographic GWs. They propagate only to a height lower than ~40 km. In contrast, clear signatures of orographic GWs extend from the surface to the mesosphere ~80 km over Greenland. In that region, in the troposphere, two cyclones are centered over Hudson Bay and Iceland; in the lower stratosphere, two sub-vortices exist where the Eurasian one approaches the CV; and in the upper stratosphere and mesosphere, a northwestward-tilting Eurasian sub-vortex exists over Greenland. A combination of northern rims of those cyclonic flow systems having different horizontal scales in each altitude form a deep westward wind that allows the upward propagation of orographic GWs. The orographic GWs over the east coast of Greenland have phase structures tilting eastward with increasing altitude and horizontal and vertical wavelengths of ~200 km and ~10 km, respectively. Their phase propagates eastward against the background westward winds, and their horizontal wavelength has a scale similar to the width of the icesheet slope. The vertical wavelength at 35 km coincides with the theoretically predicted one: $\boldsymbol{\lambda_z = 2\pi|U|/N}$, where $\boldsymbol{\lambda_z}$ = 8.1 km is obtained by substituting $\boldsymbol{|U|}$ = 27.0 m s^{-1} and $\boldsymbol{N}$ = 2.11 × 10^{-2} s^{-1}.

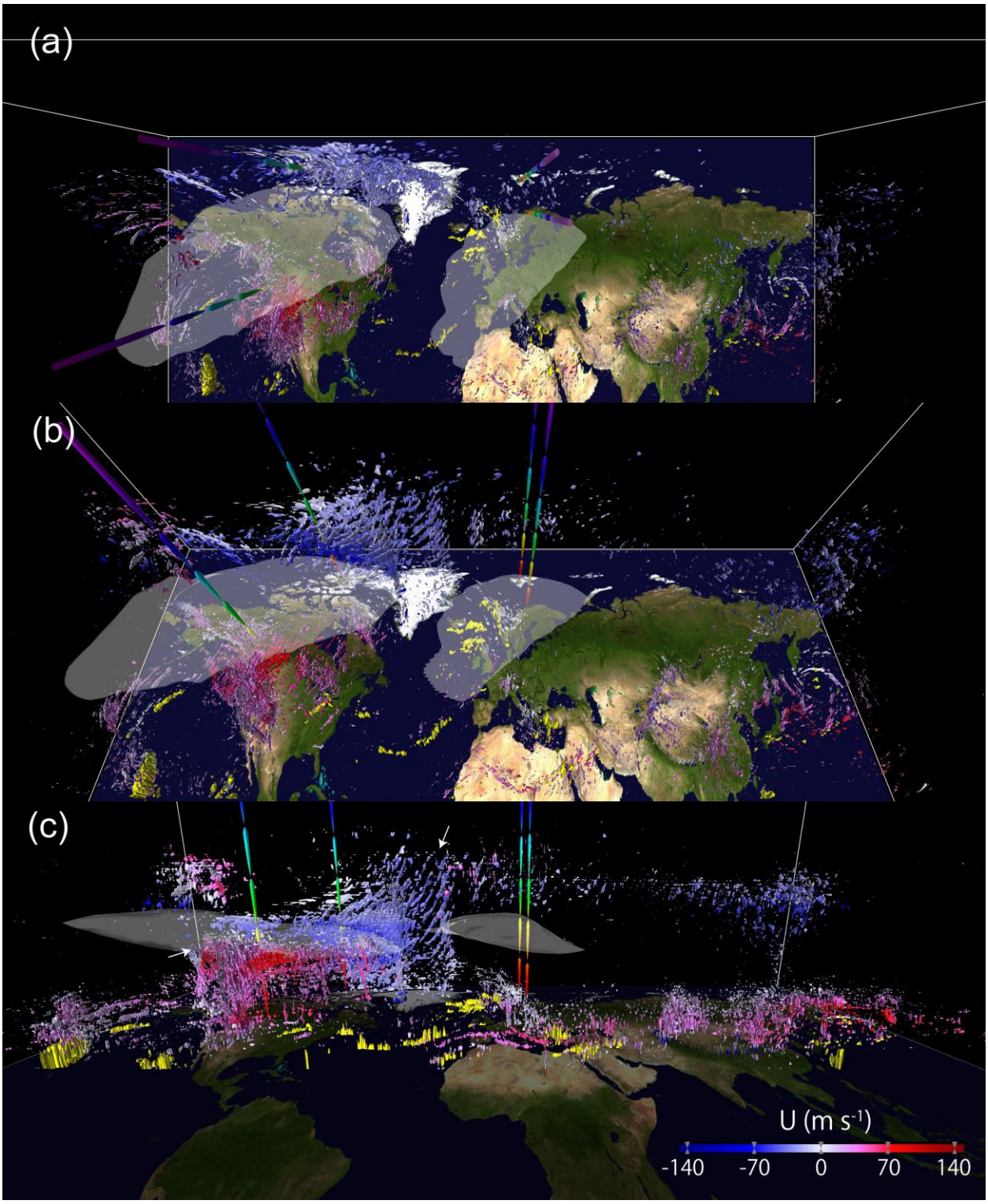

306

307 **Figure 6**. The same as Figure 1 but at 15:00UT on 15 February 2018.

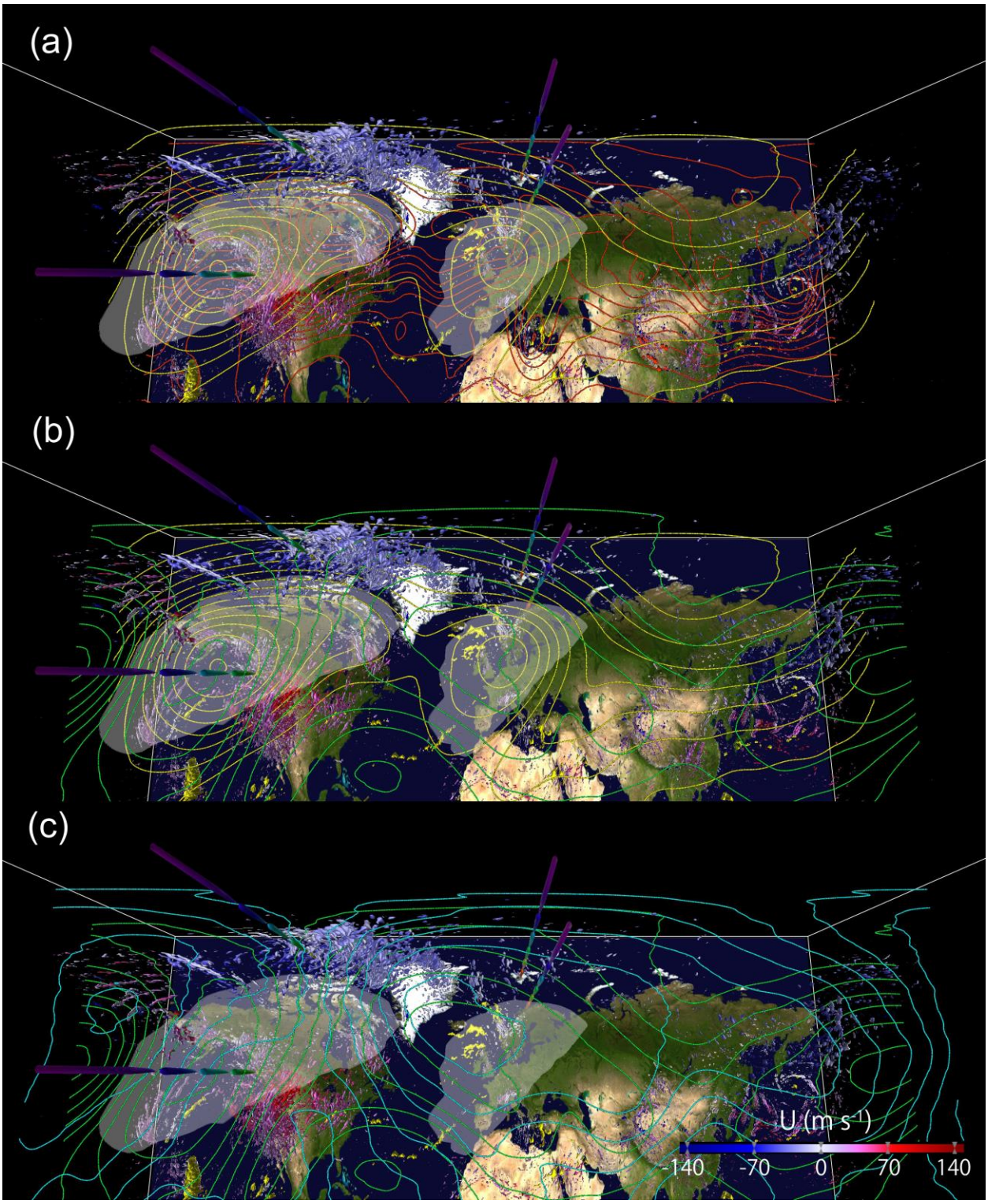

Figure 7. The same as Figure 3 but at 15:00UT on 15 February 2018.

311 Figure 8 shows a close-up view of the orographic GWs over Greenland and Ellesmere
312 Island from the southwest. The orographic GWs over the west coast of Greenland have a
313 horizontal wavelength ~90 km shorter than those over the east coast, reflecting the shorter width
314 of the ice sheet slope, which is oriented almost north-south there. Their phase propagates south-
315 southeastward against the background north-northwestward winds. Their vertical wavelength
316 increases with height from ~7 km near the surface to ~10 km in the stratosphere, which is
317 consistent with the observed increase in the background north-northwestward winds. The
318 orographic GWs over the northwest coast of Greenland and Ellesmere Island have more
319 complicated 3D phase structures due to 3D topography increased with respect to the east and
320 west coast slopes of Greenland. The dominance of more 3D GWs is expected with increasing
321 horizontal resolution of the model, which is briefly discussed below.

322

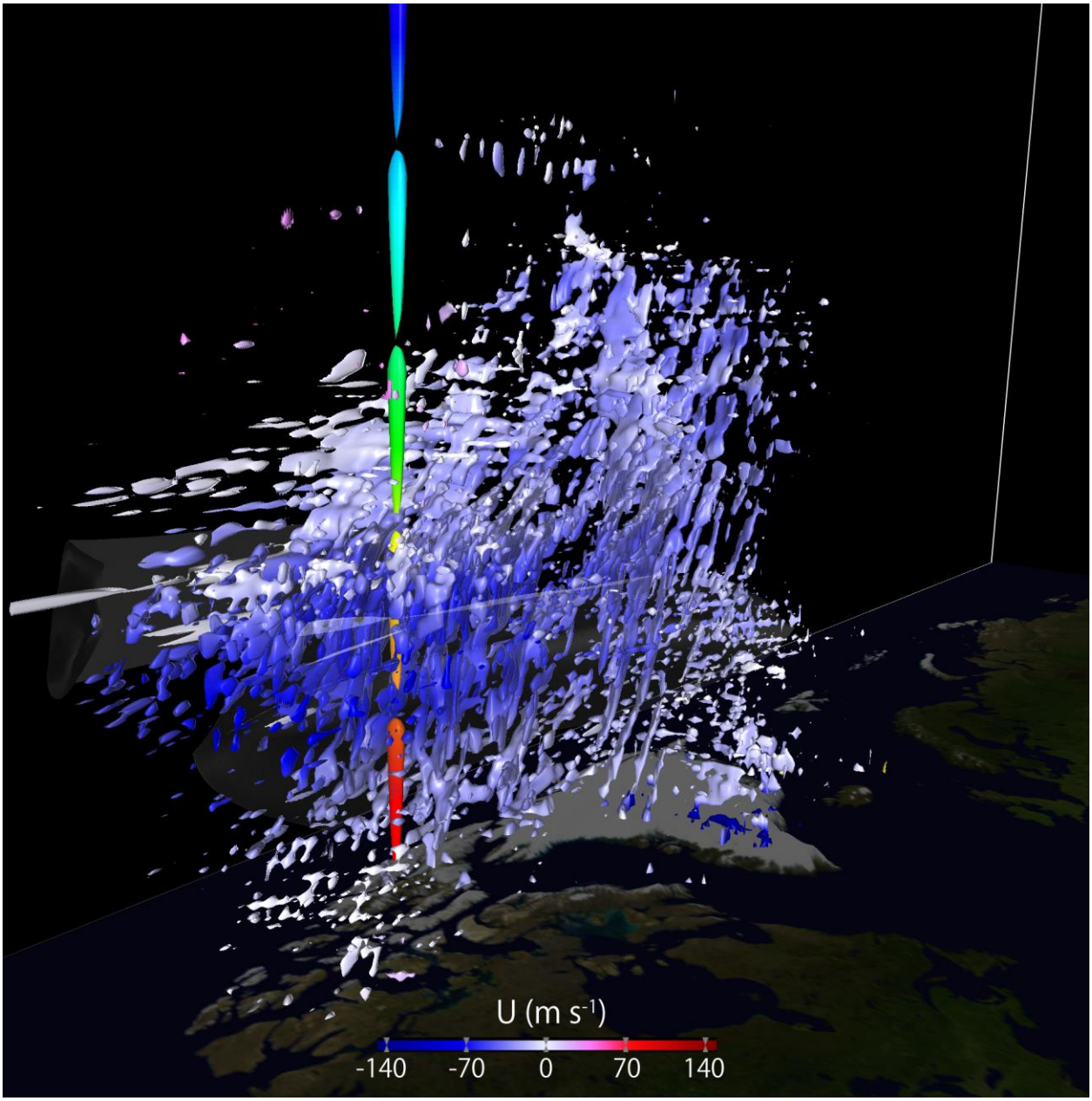

Figure 8. The same as Figure 6 but for GW signatures over Greenland and Ellesmere Island as seen from the southwest.

4. Origin and Propagation of GWs around the CV

Figures 9 illustrates the results of the 24-hour backward GW ray-tracing analysis starting from the key time 20:00UT on 11 February 2018. Figure 10 extends the analysis by the forward

GW ray tracing to 24 hours after the same key time. Here, we estimated the propagation pathways of 21 GW packets, which were initially identified near a height of 35 km at the key time. The numbers in Figures 9 and 10 denote their origins as estimated by the backward ray-tracing analysis. The GWs are categorized into several groups according to their characteristic behaviors. Table 2 summarizes their initial locations and wave parameters, as well as the directions of background winds. Table 3 provides an outlook for the results of the GW ray-tracing analyses, describing the estimated origins, propagation pathways, and dissipation of individual GWs.

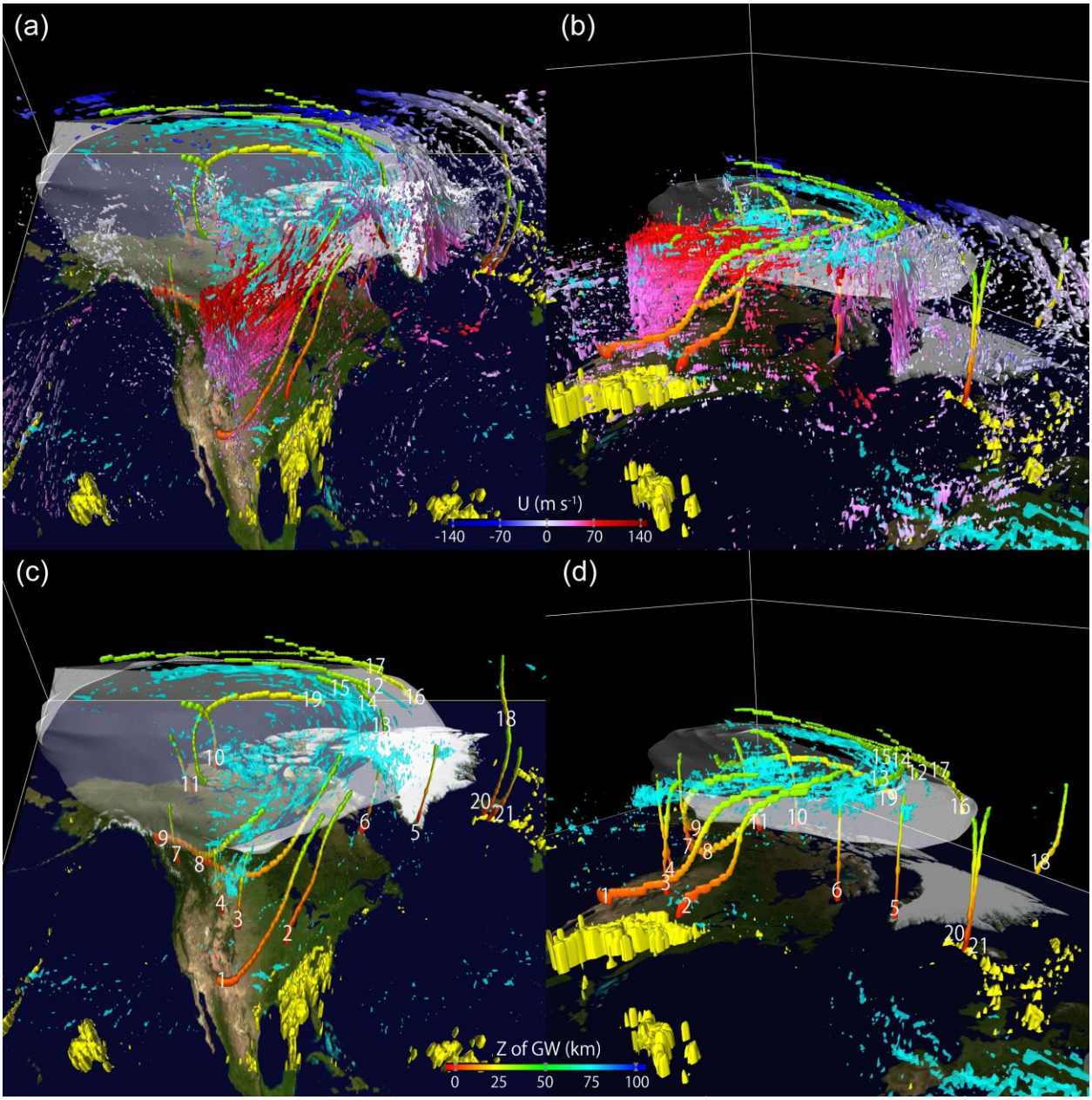

Figure 9. Results of the backward GW ray-tracing analysis starting from 35 km. (a) GW signatures and GW ray paths seen from south of the CV. The GW ray paths are colored by altitude. The light-blue transparent isosurface indicates the local Rossby number, RoL = 1.25, between 30 and 35 km. (b) The same as (a) but seen from southeast of the CV. (c) The same as (a) without GW signatures. (d) The same as (b) without GW signatures. White numbers in (c) and (d) indicate the origins of GW packets estimated by the backward GW ray-tracing analysis.

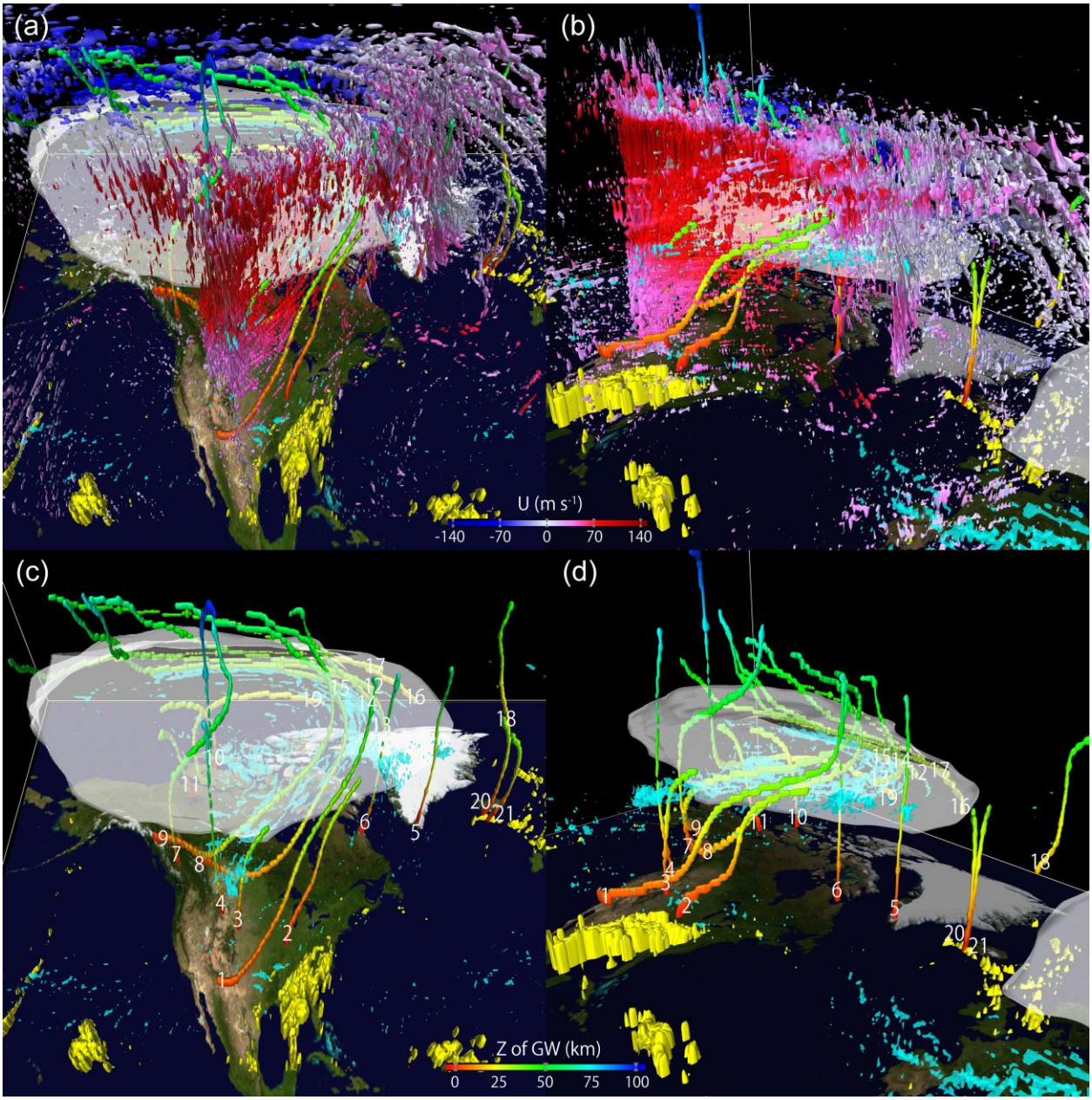

Figure 10. The same as Figure 9 but with results of the forward ray-tracing analysis added.

Table 2. Initial parameters of GW packets identified around the CV at 35 km at the key time 20:00UT on 11 February 2018. The 3rd to 7th columns show the direction of wavenumber vector ($\vec{k}$), direction of background winds ($\vec{V}_b$), horizontal wavelength (λ_h), vertical wavelength (λ_z),

353 the ratio of local inertial frequency to the intrinsic frequency of GW ($|f/\hat{\omega}|$), and the ground-based
354 phase velocity projected onto $\vec{k}$ (c), respectively.
355

No.	Initial location at 35 km	$\vec{k}$	$\vec{V}_b$	λ_h (km)	λ_z (km)	$\lvert f/\hat{\omega}\rvert$	c (m s^{-1})
A: Short vertical-wavelength GWs originating over mountains south of the CV and ascending northeastward to the eastern rim of the CV.							
1	Laurentia Plateau; 240°W 49°N	NW	NE	170	3.6	0.21	-5.0
2	Labrador Peninsula; 288°W 53°N	NW	NE	115	2.1	0.27	-8.0
B: Typical upward-propagating orographic GWs near the rim of the CV.							
3	Wyoming; 251°W 43°N	W	E	179	17.7	0.04	0.1
4	South Dakota; 260°W 43°N	NE	ENE	105	5.1	0.08	-10.8
5	South tip of Greenland; 314°W 62°N	W	NNE	127	6.6	0.12	-12.4
6	Northeastern coast of Labrador Peninsula; 297°W 58.5°N	WSW	NNE	111	21.3	0.04	-20.4
7	Northwest of Vancouver Island; 238°W 51°N	NW	ESE	120	10.8	0.05	-8.2
C: Short vertical-wavelength GWs originated near the surface in the western part of the CV and propagating long distances around the CV.							
8	Northern Labrador Peninsula; 286°W 60°N	WNW	NE	260	4.2	0.31	-1.8
9	South of Lake Winnipeg; 264°W 50°N	NW	ENE	195	3.9	0.22	-13.6
D: Upward-propagating orographic GWs originating near the surface in the northern part of the CV.							
10	Amundsen Gulf; 238°W 70°N	NNW	SW	133	3.0	0.24	2.7
11	South of Great Bear Lake; 236°W 63°N	W	ESE	98	4.2	0.13	0.4
E: Non-orographic GWs generated in situ inside and near the northern to eastern rim of the CV.							
12	North of the Queen Elizabeth Islands; 250°W 80°N	S	W	178	5.1	0.22	-15.6
13	Davis Strait; 299°W 69°N	W	N	130	2.4	0.34	-9.9
14	Baffin Bay; 292.5°W 74°N	SW	NNW	79	4.2	0.12	-12.4
15	South of Ellesmere Island; 280°W 76°N	SSW	NW	107	2.4	0.27	4.3
16	North of Ellesmere Island; 263°W 85°N	SE	NW	162	11.4	0.10	-56.1
17	Beaufort Sea; 210°W 80°N	SE	SW	126	4.2	0.20	5.7
18	Northeast coast of	W	N	102	3.3	0.21	1.0

	Greenland; 341°W 80°N						
19	Alberta; 247.5°W 55°N	SSW	ESE	180	6.9	0.12	58.6
F: Upward-propagating non-orographic GWs originating from moist diabatic heating near the ocean surface.							
20	Northwest coast of Iceland; 336°W 65°N	W	N	84	3.0	0.18	2.8
21	South of Iceland; 338°W 61°N	SW	NNE	81	5.4	0.10	-2.4

Table 3. Outlook of the GW ray-tracing analysis illustrated in Figures 9 and 10. The origin of GWs estimated by the backward ray-tracing analysis, propagation pathways during the backward and forward ray-tracing analyses, and positions for the termination of the forward ray-tracing analysis are described.

No.	Origin of GWs	Propagation pathway (backward ray tracing)	Propagation pathway and termination (forward ray tracing)
A: Short vertical-wavelength GWs originating over mountains south of the CV and ascending northeastward to the eastern rim of the CV.			
1	Western Sierra Madre Mountains 24 h ago.	Northeast propagation while rising, approaching the east rim of the CV.	Cyclonically ascending along the CV edge, terminating at a critical level near 58 km after 7 h.
2	Appalachian Mountains 9 h ago.	Same as No. 1.	NE propagation terminated shortly due to a critical level near 36 km.
B: Typical upward-propagating orographic GWs near the rim of the CV.			
3	Rocky Mountains 3.5 h ago.	Mostly upward propagation near the south rim of the CV.	Terminated at a critical level near 73 km after 3 h.
4	Rocky Mountains 3 h ago.	Same as No. 3 but slightly inclining to the northeast.	Terminated at a critical level near 39 km after 1.5 h.
5	South tip of Greenland 2.5 h ago.	Mostly upward propagation near the east rim of the CV.	Terminated at a critical level near 60 km after 4 h.
6	Northeast coast of Labrador Peninsula 3 h ago.	Same as No. 5.	Terminated at a critical level near 64 km altitude after 2 h.
7	Pacific Coast Ranges 6 h ago.	Mostly upward propagation near the west rim of the CV.	Inclined to the northeast near 50 km and terminated at a critical level near 72 km inside the CV after 12 h.
C: Short vertical-wavelength GWs originating near the surface in the western part of the CV and propagating long distances around the CV.			
8	Canadian Rockies 24 h ago.	Cyclonical ascent inside CV from the south side to the east side.	Further ascent cyclonically and terminated at a critical level near 61 km along the north rim of the CV after 13 h.
9	Canadian Coast Ranges 21 h ago.	Cyclonical ascent from the west edge to the southeast rim of the CV.	Further ascent cyclonically and terminated at a critical level near 57 km along the north rim of the CV after 14 h.
D: Upward-propagating orographic GWs originating near the surface in the northern part of the CV.			
10	North coast of Victoria Island 6.5 h ago.	Mostly upward propagation inside the CV, gradually inclining to the west-southwest.	Terminated at a critical level near 37 km in the northern part of the CV after 2 h.
11	North of Great Bear Lake	Mostly upward propagation inside	Inclined to the southwest and terminated

	5 h ago.	the CV.	at a critical level near 40 km after 4 h.
E: Non-orographic GWs generated in situ inside and near the northern to eastern rim of the CV.			
12	32 km above Baffin Bay 3.5 h ago.	Cyclonical ascent from the east edge to the north rim of the CV.	Further ascent cyclonically and terminated at a critical level near 66 km along the northwest rim of the CV after 7 h.
13	34 km above Davis Strait 1.5 h ago.	Cyclonical ascent along the east rim of the CV.	Further ascent cyclonically and terminated at a critical level near 63 km along the north rim of the CV after 11 h.
14	33 km above Baffin Bay 1 h ago.	Same as No. 13.	Further ascent cyclonically and terminated at a critical level near 56 km along the northeast rim of the CV after 2.5 h.
15	34 km above Baffin Bay 1 h ago.	Same as No. 13.	Further ascent cyclonically and terminated at a critical level near 74 km along the northwest rim of the CV after 10.5 h.
16	24 km above Greenland 5 h ago.	Cyclonical ascent from the east edge to the north rim of the CV.	Further ascent cyclonically and terminated at a critical level near 55 km along the northwest rim of the CV after 3.7 h.
17	31 km above northern Greenland 4.5 h ago	Cyclonical ascent from the northeast edge to the northwest rim of the CV.	Further ascent cyclonically and terminated at a critical level near 55 km along the northwest rim of the CV after 5.5 h.
18	20 km above the Greenland Sea 5 h ago.	Northward ascent about 300 km from the east rim of the CV.	Terminated at a critical level near 47 km altitude about 300 km from the northeast rim of the CV after 7 h.
19	21 km above Ellesmere Island 24 h ago (probably generated earlier).	Cyclonical ascent inside CV from the northeast part to the central to southern part of the CV.	Changed to mostly upward propagation and terminated at a critical level near 92 km in the central to southern part of the CV after 4.3 h.
F: Upward-propagating non-orographic GWs originating from moist diabatic heating near the ocean surface.			
20	South of Iceland 5.5 h ago.	Mostly upward propagation inclining slightly to the north-northwest.	Terminated at a critical level near 36 km after 1 h.
21	South of Iceland 3.8 h ago.	Same as No. 20 but with faster ascent.	Terminated at a critical level near 38 km after 2 h.

Group A consists of short vertical-wavelength GWs generated over the mountains south of the southern rim of the CV; these GWs propagate long distances to the northeast and approach the eastern rim of the CV. GW packet #1, initially identified over the Laurentia Plateau at the key time, has a northwestward phase propagation direction through northeastward background winds, ~170 km horizontal and 3.6 km vertical wavelengths, and an intrinsic frequency about 5 times higher than the local inertial frequency. The backward and forward ray-tracing analyses revealed that this GW packet originated over the Western Sierra Madre Mountains 24 hours before the key time, obliquely ascended northeastward to approach the eastern rim of CV, and

then changed the propagation direction counterclockwise, being refracted and advected by CV winds; eventually, it reached its critical level near 58 km along the northern rim of the CV 7 hours after it crossed the 35-km level. GW packet #2 has shorter horizontal and vertical wavelengths and a lower frequency than those of #1. It originated over the Appalachian Mountains and similarly propagated over a long distance northeastward and reached its critical level along the eastern rim of the CV at 36 km. Although GW packets #1 and #2 originated over mountains, they obviously differ from the typical upward-propagating, quasi-stationary orographic GWs. They might have been orographic GWs whose wave parameters were strongly modulated through refraction in strongly sheared CV winds (e.g., Sato et al., 2012) or secondarily generated GWs emitted from the wave breaking of the primary orographic GWs generated directly over the mountains (e.g., Satomura & Sato, 1999).

The typical upward-propagating, quasi-stationary orographic GWs identified near the rim of the CV are classified as Group B. Two of them originated above the Rocky Mountains 3-3.5 hours before the key time. GW packet #3 had a westward wave phase propagation direction against the background of eastward winds and propagated mostly upward near the southern rim of the CV. It had an almost zero ground-based phase speed, ~180 km and ~18 km horizontal and vertical wavelengths, respectively, and an intrinsic frequency more than 20 times higher than the local inertial frequency near 35 km. The vertical wavelength coincides with the theoretically predicted one: $\boldsymbol{\lambda_z = 2\pi|U|/N}$, where $\boldsymbol{\lambda_z}$ = 17.8 km is obtained by substituting $\boldsymbol{|U|}$ = 69.1 m s^{-1} and $\boldsymbol{N}$ = 2.44 × 10^{-2} s^{-1}. It propagated into the mesosphere and reached its critical level near 73 km 3 hours after the key time. GW packet #4 had a northeastward wave phase propagation that corresponds well to the major direction of the topography. It had shorter horizontal (~115 km) and vertical (~2.1 km) wavelengths, and its intrinsic frequency was about 20% lower compared to #3. It propagated upward with a slightly northeastward incline, probably due to wave phase refraction by the horizontal shear of background CV winds, and reached its critical level near 39 km. Three GW packets were also identified at the 35-km level, near the south tip of Greenland (#5), the northeastern coast of the Labrador Peninsula (#6), and the northwest of Vancouver Island (#7). These are orographic GWs having long vertical wavelengths that propagated upward from the surface to the lower mesosphere through the deep CV winds. An interesting exception is the last case, GW #7, which changed its propagation direction in the upper stratosphere and mesosphere, inclining to the northeast and propagating to the center of the

CV. The strong horizontal shears of background winds associated with the cyclonic flow of the CV likely caused the refraction of the GW wavenumber vector in the upper stratosphere and mesosphere.

The GWs in Group C have similar characteristics to those in Group A. They had short vertical wavelengths generated near the surface, and cyclonically propagated over long distances along the CV. The two GW packets are identified at the 35-km level. GW packet #8, initially found over the northern Labrador Peninsula, had a west-northwest wave phase propagation direction partly against the northeastward background winds. This packet had ~260 km horizontal and ~4.2 km vertical wavelengths, and its intrinsic frequency was about 3 times as high as the local inertial frequency. The backward and forward ray-tracing analyses reveal that this GW packet originated over the Canadian Rocky Mountains inside the CV 24 hours before the key time and ascended cyclonically from the southern side to eastern side of the CV. This GW was further refracted and advected by CV winds, reached 35 km, ascended cyclonically, and then terminated at a critical level near 61 km along the northern rim of the CV 13 hours after it crossed the 35-km level. The other GW packet, #9, initially found over the south of Lake Winnipeg at 35 km, similarly ascended cyclonically along the rim of the CV. It originated from the Canadian Coast Ranges near the eastern rim of the CV, propagated over 3/4 of the circumference of the CV, and dissipated at its critical level near 57 km along the northern rim of the CV.

Two upward-propagating orographic GW packets (#10 and #11), classified as Group D, are found in the northern part of CV, where the background horizontal winds had large horizontal and vertical shears. The anti-cyclonic eastward-to-southward background winds were dominant in the troposphere, which were covered by the cyclonic westward to southward background winds in the stratosphere (Fig. 5a). GW packet #10, found over the Amundsen Gulf at 35 km, had a north-northwestward wave phase propagation direction partly against the southwestward background winds. It had ~133 km horizontal and ~3.0 km vertical wavelengths and an intrinsic frequency about 4 times as high as the local inertial frequency. According to the background ray-tracing analysis, this GW packet originated over the north coast of Victoria Island below the northern part of CV about 6.5 hours before the key time, propagated upward, and gradually inclined to the west-southwest with height, being refracted and advected by the

sheared background winds. The propagation terminated at a critical level near 37 km in the central to northwestern part of the CV 2 hours after it crossed the 35-km level. GW packet #11, initially found over the south of Great Bear Lake, had shorter ~100 km horizontal and longer ~4.2 km vertical wavelengths at 35 km. It had a westward phase propagation direction against the east-southeastward CV winds, propagating mostly upward with a slight inclination to the south from the surface to near 40 km, where it encountered its critical level.

We now focus on the area around the east to north rim of the CV, where several GWs that were likely generated in situ can be recognized. Group E GWs propagated cyclonically along the CV winds and have horizontal wavelengths of 80-180 km with phase structures aligned parallel to the background winds. Some of them had short wave lifetimes of ~1 hour, as illustrated by short GW ray segments in Fig. 9, from the time of their generation to their identification at 35 km. They probably originated from a spontaneous adjustment of flow imbalance associated with the deformation of CV winds, as illustrated by the light-blue isosurface of a large RoL between 30 and 35 km. GW packet #12, found over north Queen Elizabeth Island at 35 km, had a southward wave phase propagation direction, which was perpendicular to the westward background winds near the northern rim of the CV. It had ~180 km horizontal and ~5.1 km vertical wavelengths, and its intrinsic frequency was about 5 times as high as the local inertial frequency. This non-orographic GW is estimated to have originated from a location 32 km above Baffin Bay near the northern rim of the CV 3.5 hours before the key time, and it obliquely propagated along the CV winds and eventually encountered a critical level near 66 km near the northwestern rim of the CV 7 hours after it crossed the 35-km level. Other in situ-generated non-orographic GWs found near the east to north rim of the CV, #13-17, show behavior similar to that of #12, in which they originated from the large RoL regions, obliquely propagated along the cyclonic CV winds, and dissipated at heights of 55-74 km in the lower mesosphere.

Among them, the behavior of GW packet #19 identified inside the CV was of great interest, as it exhibited a complicated 3D propagation inside the CV. It came from about 21 km above Ellesmere Island 24 hours before it was identified over Alberta at the 35-km level, first propagating almost horizontally and slightly upward, cyclonically propagating around half the CV interior in 24 hours, and then suddenly changing its propagation direction to mainly upward,

reaching as high as ~92 km in 4.3 hours. The 3D structures of CV winds no doubt played a central role in the refraction of the wavenumber vector and advection of wave energy to cause such a characteristic propagation. That GW packet had a south-southwestward wave phase propagation partly against the east-southeastward background winds over Alberta at 35 km, with ~180 km horizontal and ~6.9 km vertical wavelengths, and an intrinsic frequency about 8 times as high as the local inertial frequency. The background eastward winds rapidly strengthened with increasing height in the upper stratosphere over Alberta and were associated with the slight southwestward inclination of the CV (Fig. 5b), which increased the vertical group velocity of the GW.

Finally, two GW packets #20 and #21 found over south Iceland are estimated to be non-orographic GWs emitted from near-surface moist diabatic heating. They had a similar horizontal wavelength of ~85 km with slightly different directions for the wave phase propagation and background winds at 35 km. GW packet #20 (#21) had a shorter (longer) vertical wavelength of 3.0 km (5.4 km) and a lower (higher) intrinsic frequency about 5 times (10 times) as high as the local inertial frequency. They were generated about 5.5 hours and 3.8 hours before they crossed the 35 km level and shortly encountered their critical levels near 36 km and 38 km, respectively.

5. Summary and discussion

The GWs during the February 2018 SSW were simulated using the T639L340 whole neutral atmosphere GCM and their characteristic morphology around the drastically evolving polar vortex was revealed by 3D visualization and ray-tracing analyses. The 3D morphology of simulated GWs was described during the three key days representing the pre-SSW, the mature stage for the vortex splitting, and the late SSW. The combination of strong winds along the polar vortex edge and underneath tropospheric winds with similar wind directions constituted a deep waveguide for the upward-propagating GWs, forming GW hot spots in the middle atmosphere. The GW hot spots were confined to over North America and Greenland with the development of the SSW, and they included the typical upward-propagating orographic GWs with relatively long vertical wavelengths. Different types of characteristic GW signatures were also recognized around the CV. The GWs having short vertical wavelengths formed near the surface and obliquely propagated over long distances on the CV winds. The non-orographic GWs with short

vertical wavelengths formed in the middle stratosphere through the spontaneous adjustment of flow imbalance around the CV. Those GWs cyclonically ascended into the mesosphere along the CV winds. Video 1 visualizes the result of hindcast simulation that includes the splitting of the NH polar vortex, demonstrating the dramatic changes in the large-scale flow patterns and GW morphology during the SSW.

<Video 1 should be embedded here. It was uploaded separately because of the 100MB limit of GEMS.>

Video 1. 3D animation of GW signatures and the NH polar vortices in an 8 day hindcast simulation from 00:00UT on 8 February 2018. The period from 00:00UT on 9 February 2018 to 06:40UT on 14 February 2018 is displayed in 10-minute interval timeframes. The length of animation is 42 seconds. The DIV isosurface value is -7.5×10^{-5}.

This study achieved its goal of illustrating the behavior of GWs associated with the SSW through 3D visualization by focusing on their morphological features. Compared with Limpasuvan et al. (2011), the model has a lower horizontal resolution but a wider horizontal and vertical domain, which allowed us to obtain new images of GWs around the CV. It is a future task to investigate the GW morphology of other SSW events, seasons, and locations, including higher altitudes, and the momentum transport by GWs with this model. As mentioned in Section 2, the GWs shown here were not hindcast from observed initial values for GWs, and their credibility depends on the ability of the GCM to simulate GWs, as well as the reasonableness of the large-scale fields of the data assimilation system used for the initialization of the large-scale fields of the GCM. The dependence of simulated GWs on the horizontal, vertical, and temporal resolutions of GCMs has been actively studied (e.g., Hamilton et al., 1999; Shutts & Vosper, 2011; Watanabe et al., 2015), and recent studies suggest that a horizontal resolution of less than 3 km is required to accurately represent small-scale GWs (Kruse et al., 2022). Because it is impossible to perform global whole neutral atmosphere simulations at sub-kilometer resolution, even with the current computing environment and the latest models, we will briefly compare and

519 discuss the results of the prototype GCM simulations at T2559L340 resolution, the results of
520 T639L340 resolution described in this study, and the latest high-resolution reanalysis data, ERA5,
521 provided at a 0.25° horizontal resolution, as a best effort. The T2559L340 GCM was initialized
522 with procedures similar to those used for the T639L340 GCM. In this case, the n = 0-40 spectral
523 components of the T2559L340 GCM were nudged to those output from the T639L340 hindcast
524 for 18 hours from 20:00UT on 10 February 2018, during which n = 41-2,559 spectral
525 components formed spontaneously. The results presented here demonstrate the end of a 6-hour
526 free run following the spectral nudging. The time is 20:00UT on 11 February 2018.

527 Figure 11 compares the GW signatures around the CV in the three data sets. Note that the
528 DIV isosurface values shown in the figure are different because of the different magnitudes of
529 GW amplitudes among the data sets, which become larger with increasing spatial resolution. The
530 amplitudes of GWs in the T639L340 model are about twice as large as those in the ERA5 data
531 set, and the GW amplitudes in the T2559L340 model are about three times as large as those in
532 T639L340. The ERA5 has the lowest horizontal and vertical resolutions and exhibits GW
533 signatures similar to the upward-propagating, long-vertical-wavelength orographic GWs and
534 obliquely propagating short-vertical-wavelength GWs noted in this study. As the horizontal
535 resolution increases, there is a clear tendency for GWs with finer horizontal wavelengths to
536 dominate. Nonetheless, the region where vertically propagating GWs exist remains unchanged.
537 This indicates that the contribution of the background wind is important.

538 When we focus on the short-vertical-wavelength GWs cyclonically ascending around the
539 CV highlighted in this study, the GW morphology of the T639L340 GCM was generally
540 reproduced by the higher-resolution T2559L340 GCM, implicitly supporting the credibility of
541 the present GW simulations with the T639L340 GCM. The behaviors of GWs presented in this
542 study also depend on the 1-hour temporal average before output from the model, obscuring high-
543 frequency GWs existing in the model, which may play non-negligible roles in the momentum
544 budget in the middle atmosphere (see Video 1 for 10 minutes average of DIV). However,
545 observational studies have reported that GWs with a period longer than 3 h are mainly
546 responsible for momentum transport, at least in the summer polar mesosphere (Sato et al., 2017).
547 Which GW frequencies are important for momentum transport in each latitude and altitude

region has not yet been clarified. Further high-resolution modeling and analyses in the future should clarify these points.

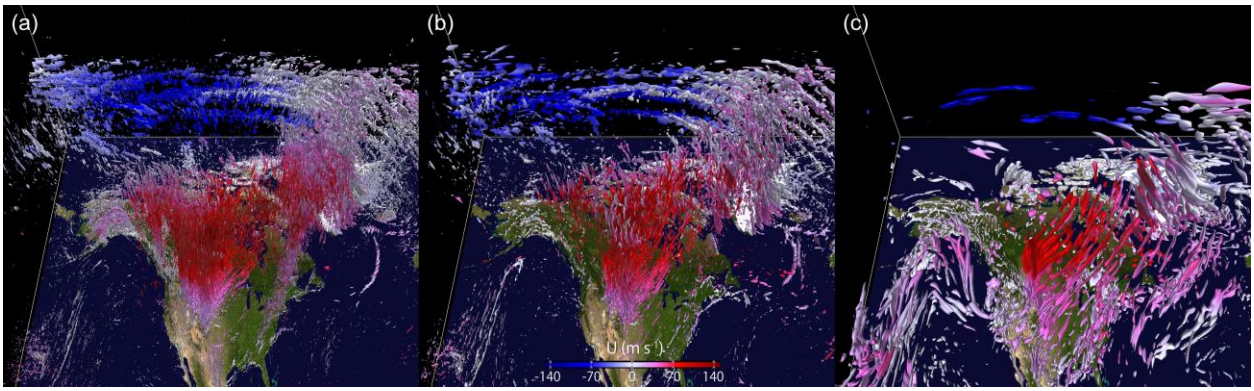

Figure 11. 3D view of GW signatures in (a) T2559L340 GCM, (b) T639L340 GCM, and (c) ERA5 at 20:00UT on 11 February 2018. In each panel, the DIV isosurface values are -1.2×10^{-4}, -6×10^{-5}, and -2×10^{-5}, respectively.

We also briefly discuss the possibility of finding GWs with characteristics similar to those simulated by GCMs with existing observational data. For upward-propagating orographic GWs having long vertical wavelengths, it would be possible to use data from various instruments. It would be interesting to detect GWs with complex horizontal phase structures using AIRS data, and to discuss the relationship between the vertical phase structure of the detected GWs and the background fields using radiosonde data. In comparison, it would be more difficult to detect and trace GWs with short vertical wavelengths propagating over long distances (e.g., Alexander & Barnet, 2007). The operational radiosonde data are useful in the troposphere and lower stratosphere, but their limited spatio-temporal resolution means that even if GWs similar to those of the simulation exist, they might be missed. The high vertical resolution of the U.S. radiosonde data set may be helpful due to its wide spatial coverage (Wang & Geller, 2003).

In the upper stratosphere and lower mesosphere, fewer instruments can detect GWs having vertical wavelengths of 2-4 km. Mesosphere-stratosphere-troposphere radars and lidars

are advantageous for temporal and vertical resolutions, although no such data are available over North America during the February 2018 SSW. Meanwhile, at altitudes higher than those targeted in this study, data from the ICSOM intensive observation campaign, obtained by the Eureka meteor radar and the Saskatoon Medium Frequency radar, are available and will be used to validate the model. Global navigation satellite system occultation observations may provide the best spatio-temporal coverage (e.g., Luo et al., 2021).

It is more difficult to capture the same wave packet at different times and locations by observations. Even with this study's dense GCM simulation data combined with the 3D visualization and ray-tracing analysis, it was difficult because GWs change their parameters during propagation, and because various GWs emitted from various sources overlap. Although it is a unique feature of this study, some of the important results were partly based on subjective visual inspections of the 3D wave parameters and visual traces of propagating GW packets, which were complementary to the 3D ray-tracing analysis. Development and/or employment of new analysis methods are expected to extend the utility of our method. For example, application of machine learning approaches would be promising to automatically detect large-amplitude GWs; estimate and label their wave parameters, propagation pathways, and sources; and archive relationships between GWs and the background fields, which we did manually in this study (e.g., an extension of Matsuoka et al., 2020).

We hope that the results and discussions of this GW simulation study focusing on their morphology during an SSW will inspire new observational, data analysis, and modeling studies.

Acknowledgments

This study was supported by the Japan Science and Technology Agency Core Research for Evolutional Science and Technology (Grant No. JPMJCR1663) and the Integrated Research Program for Advancing Climate Models (TOUGOU) Grant No. JPMXD0717935715 from the Japan Ministry of Education, Culture, Sports, Science and Technology (MEXT). The simulations in this study were performed using the Earth Simulator at the Japan Agency for Marine-Earth Science and Technology (JAMSTEC) and all graphs are created using the VAPOR software, version 2.6.0. The authors would like to thank Dr. Fuyuki Saito, Dr. Koji Ogochi, and the staff of

598 the Center for Earth Information Science and Technology at JAMSTEC and NEC for their help
599 in increasing the resolution of the GCM and optimizing it for the Earth Simulator.
600

601 **Open Research**

602 All the raw data, metadata, and saved session files necessary for re-producing the figures in this
603 paper are available at https://doi.org/10.5281/zenodo.5793119. For legal reasons, the source code
604 for the GCM cannot be publicly released. It has been (will be) made available to the editor and
605 reviewers, and is available to anyone who contacts the corresponding author. VAPOR version
606 2.6.0 is available at https://vapor.readthedocs.io/en/readthedocs/downloads.html#vapor-2. The
607 ERA5 hourly data on pressure levels from 1979 to present is available at
608 https://cds.climate.copernicus.eu/cdsapp#!/dataset/10.24381/cds.bd0915c6?tab=overview.
609

610 **References**

611 Alexander, M. J., & Barnet, C. (2007), Using satellite observations to constrain
612 parameterizations of gravity wave effects for global models. *Journal of the Atmospheric*
613 *Sciences*, *64*(5), 1652–1665. doi:10.1175/JAS3897.1.
614 Amemiya, A., & Sato, K. (2016), A new gravity wave parameterization including three-
615 dimensional propagation. *Journal of the Meteorological Society Japan*, *94*, 237–256.
616 doi:10.2151/jmsj.2016-013.
617 Charlton, A. J., & Polvani, L. M. (2007), A new look at stratospheric sudden warmings. Part I:
618 Climatology and modeling benchmarks. *Journal of Climate*, *20*, 449–469.
619 doi:10.1175/JCLI3996.1.
620 Fritts, D. C., & Alexander, M. J. (2003), Gravity wave dynamics and effects in the middle
621 atmosphere. *Review of Geophysics*, *41*, 1003. doi:10.1029/2001RG000106, 1.
622 Hamilton, K., Wilson, R. J., & Hemler, R. S. (1999), Middle atmosphere simulated with high
623 vertical and horizontal resolution versions of a GCM: Improvements in the cold pole bias and
624 generation of a QBO-like oscillation in the tropics. *Journal of the Atmospheric Sciences*, *56*(22),
625 3829–3846. doi:10.1175/1520-0469(1999)056<3829:MASWHV>2.0.CO;2.
626 Harada, Y., Sato, K., Kinoshita, T., Yasui, R., Hirooka, T., & Naoe, H. (2019), Diagnostics of a
627 WN2-type major sudden stratospheric warming event in February 2018 using a new three-

628 dimensional wave activity flux. *Journal of Geophysical Research: Atmospheres*, *124*, 6120–
629 6142. doi:10.1029/2018JD030162.
630 Hersbach, H., Bell, B., Berrisford, P., Hirahara, S., Horányi, A., Muñoz-Sabater, J., et al. (2020),
631 The ERA5 global reanalysis. *Quarterly Journal of the Royal Meteorological Society*, *146*(730),
632 1999–2049. doi:10.1002/qj.3803.
633 Koshin, D., Sato, K., Kohma, M., & Watanabe, S. (2021), An update on the 4D-LETKF data
634 assimilation system for the whole neutral atmosphere. *Geoscientific Model Development*
635 *Discussion*. doi:10.5194/gmd-2020-381.
636 Koshin, D., Sato, K., Miyazaki, K., & Watanabe, S. (2020), An ensemble Kalman filter data
637 assimilation system for the whole neutral atmosphere. *Geoscientific Model Development*, *13*,
638 3145–3177. doi:10.5194/gmd−13-3145-2020.
639 Kruse, C. G., Alexander, M. J., Hoffmann, L., van Niekerk, A., Polichtchouk, I., Bacmeister, J.
640 T., et al. (2022), Observed and modeled mountain waves from the surface to the mesosphere near
641 the Drake Passage. *Journal of the Atmospheric Sciences*, in press. doi:10.1175/JAS-D-21-0252.1.
642 Li, S., Jaroszynski, S., Pearse S., Orf, L. & Clyne, J. (2019), VAPOR: A visualization package
643 tailored to analyze simulation data in Earth system science. *Atmosphere*, *10*(9), 488.
644 doi:10.3390/atmos10090488.
645 Limpasuvan, V., Alexander, M. J., Orsolini, Y. J., Wu, D. L., Xue, M., Richter, J. H., &
646 Yamashita, C. (2011), Mesoscale simulations of gravity waves during the 2008–2009 major
647 stratospheric sudden warming. *Journal of Geophysical Research: Atmospheres*, *116*, D17104.
648 doi:10.1029/2010JD015190.
649 Luo, J., Hou, J., & Xu, X. (2021), Variations in stratospheric gravity waves derived from
650 temperature observations of multi-GNSS radio occultation missions. *Remote Sensing*, *13*, 4835.
651 doi:10.3390/rs13234835.
652 Marks, C. J., & Eckermann, S. D. (1995), A three-dimensional nonhydrostatic ray-tracing model
653 for gravity waves: Formulation and preliminary results for the middle atmosphere. *Journal of the*
654 *Atmospheric Sciences*, *52*(11), 1959–1984. doi:10.1175/1520-
655 0469(1995)052<1959:ATDNRT>2.0.CO;2.
656 Matsuoka, D., Watanabe, S., Sato, K., Kawazoe, S., Yu, W., & Easterbrook, S. (2020),
657 Application of deep learning to estimate atmospheric gravity wave parameters in reanalysis data
658 sets. *Geophysical Research Letters*, *47*, e2020GL089436. doi:10.1029/2020GL089436.

Matthewman, N. J., Esler, J. G., Charlton-Perez, A. J., & Polvani, L. M. (2009), A new look at stratospheric sudden warmings. Part III: Polar vortex evolution and vertical structure. *Journal of Climate*, *22*(6), 1566–1585. doi:10.1175/2008JCLI2365.1.

Okui, H., Sato, K., Koshin, D., & Watanabe, S. (2021), Formation of a mesospheric inversion layer and the subsequent elevated stratopause associated with the major stratospheric sudden warming in 2018/19. *Journal of Geophysical Research: Atmospheres*, *126*, e2021JD034681. doi:10.1029/2021JD034681.

Perrett, J. A., Wright, C. J., Hindley, N. P., Hoffmann, L., Mitchell, N. J., Preusse, P., et al. (2021), Determining gravity wave sources and propagation in the Southern Hemisphere by ray-tracing AIRS measurements. *Geophysical Research Letters*, *48*, e2020GL088621. doi:10.1029/2020GL088621.

Sato, K., & Yoshiki, M. (2008), Gravity wave generation around the polar vortex in the stratosphere revealed by 3-hourly radiosonde observations at Syowa Station. *Journal of the Atmospheric Sciences*, *65*(12), 3719–3735. doi:10.1175/2008JAS2539.1.

Sato, K., Kohma, M., Tsutsumi, M., & Sato, T. (2017), Frequency spectra and vertical profiles of wind fluctuations in the summer Antarctic mesosphere revealed by MST radar observations. *Journal of Geophysical Research: Atmospheres*, *122*, 3–19. doi:10.1002/2016JD025834.

Sato, K., Tateno, S., Watanabe, S., & Kawatani, Y. (2012), Gravity wave characteristics in the Southern Hemisphere revealed by a high-resolution middle-atmosphere general circulation model. *Journal of the Atmospheric Sciences*, *69*(4), 1378–1396. doi:10.1175/JAS-D-11-0101.1.

Satomura, T., & Sato, K. (1999), Secondary generation of gravity waves associated with the breaking of mountain waves. *Journal of the Atmospheric Sciences*, *56*(22), 3847–3858. doi:10.1175/1520-0469(1999)056<3847:SGOGWA>2.0.CO;2.

Shibuya R., Sato, K., Tsutsumi, M., Sato, T., Tomikawa, Y., Nishimura, K., & Kohma, M. (2017), Quasi-12h inertia-gravity waves in the lower mesosphere observed by the PANSY radar at Syowa Station (39.6E, 69.0S). *Atmospheric Chemistry and Physics*, *17*, 6455–6476. doi:10.5194/acp-2016-813.

Shutts, G. J., & Vosper, S. B. (2011), Stratospheric gravity waves revealed in NWP model forecasts. *Quarterly Journal of the Royal Meteorological Society*, *137*(655), 303–317. doi:10.1002/qj.763.

689 Song, I.-S., & Chun, H.-Y. (2008), A Lagrangian spectral parameterization of gravity wave drag
690 induced by cumulus convection. *Journal of Atmospheric Science*, *65*, 1204–1224.
691 doi:10.1175/2007JAS2369.1.
692 Wang, L., & Geller, M. A. (2003), Morphology of gravity-wave energy as observed from 4 years
693 (1998–2001) of high vertical resolution U.S. radiosonde data. *Journal of Geophysical Research:*
694 *Atmospheres*, *108*, D16, 4489. doi:10.1029/2002JD002786.
695 Watanabe, S., and Miyahara, S. (2009), Quantification of the gravity wave forcing of the
696 migrating diurnal tide in a gravity wave–resolving general circulation model. *Journal of*
697 *Geophysical Research: Atmospheres*, *114*, D07110. doi:10.1029/2008JD011218.
698 Watanabe, S., Sato, K., Kawatani, Y., & Takahashi, M. (2015), Vertical resolution dependence
699 of gravity wave momentum flux simulated by an atmospheric general circulation model.
700 *Geoscientific Model Development*, *8*, 1637–1644. doi:10.5194/gmd-8-1637-2015.
701 Wright, C. J., Hindley, N. P., Hoffmann, L., Alexander, M. J., & Mitchell, N. J. (2017),
702 Exploring gravity wave characteristics in 3-D using a novel S-transform technique: AIRS/Aqua
703 measurements over the Southern Andes and Drake Passage. *Atmospheric Chemistry and Physics*,
704 *17*, 8553–8575. Doi:10.5194/acp-17-8553-2017.